Interactions between Nitric Oxide and Indoleamine 2,3-Dioxygenase†

Ben J. Samelson-Jones and Syun-Ru Yeh*

Department of Physiology and Biophysics, Albert Einstein College of Medicine of Yeshiva University, Bronx, New York 10461

Received January 23, 2006; Revised Manuscript Received May 15, 2006

ABSTRACT: Indoleamine 2,3-dioxygenase (IDO) is a heme-containing enzyme, which catalyzes the initial and rate-determining step of L-tryptophan (L-Trp) metabolism via the kynurenine pathway in nonhepatic tissues. Similar to inducible nitric oxide synthase (iNOS), IDO is induced by interferon-γ and lipopolysaccharide in the inflammatory response. In vivo studies indicate that the nitric oxide (NO) produced by iNOS inhibits IDO activity by directly interacting with it and by promoting its degradation through the proteasome pathway. In this work, the molecular mechanisms underlying the interactions between NO and human recombinant IDO (hIDO) were systematically studied with optical absorption and resonance Raman spectroscopies. Resonance Raman data show that the heme prosthetic group in the NO-bound hIDO is situated in a unique protein environment and adopts an out-of-plane deformed geometry that is sensitive to L-Trp binding. Under mildly acidic conditions, the proximal heme iron−His bond is prone to rupture, resulting in a five-coordinate (5C) NO-bound species. The bond breakage reaction induces significant conformational changes in the protein matrix, which may account for the NO-induced inactivation of hIDO and its enhanced proteasome-linked degradation in vivo. Moreover, it was found that the NO-induced bond breakage reaction occurs more rapidly in the ferrous protein than in the ferric protein and is fully inhibited by L-Trp binding. The spectroscopic data presented here not only provide the first glimpse of the possible regulatory mechanism of hIDO by NO in the cell at the molecular level, but they also suggest that the NO-dependent regulation can be modulated by cellular factors, such as the NO abundance, pH, redox environment, and L-Trp availability.

Indoleamine 2,3-dioxygenase (IDO), a heme-containing enzyme with a molecular weight of 45 kD (*1*), catalyzes the initial and rate-determining step of L-tryptophan (L-Trp) metabolism via the kynurenine pathway in nonhepatic tissues (*2*). The ferrous form of the enzyme inserts molecular oxygen on the second and third carbons of the indole moiety of L-Trp, which produces L-*N*-formylkynurenine that subsequently degrades to L-kynurenine as illustrated in Scheme 1 (*3*). The ferric protein may be activated by using superoxide as the oxidizing agent, but its physiological significance remains unclear (*4*, *5*). In addition to L-Trp, IDO also catalyzes pyrrole ring cleavage reactions of a group of indoleamine derivatives, including D-Trp, tryptamine, serotonin, and melatonin (*6*, *7*).

IDO has been found to exhibit disparate physiological functions. In the eye lens, metabolites of L-Trp act as UV filters to protect the retina from high-energy photons. However, under pathological conditions, these metabolites may accumulate and form adducts with lens proteins, leading to senile cataracts (*8*, *9*). In the immune system, IDO is induced by interferon-γ (IFN-γ)[1] (*10*) or lipopolysaccharide (LPS) (*11*) and was found to be essential in pathogen clearance of a number of microorganisms (*12*−*18*). Paradoxically, IDO also induces immune tolerance; for example, it was implicated in the maternal tolerance to allogenic fetuses (*19*) and in the pathological immune tolerance to cancers (*20*, *21*). Along the same lines, IDO was suggested

Scheme 1: Reaction Catalyzed by IDO

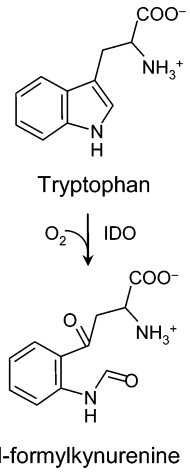

† This work is supported by NIH Grant HL65465 to S.-R.Y. B.J.S.-J. is supported by the Medical Scientist Training Program (GM07288) and the Molecular Biophysics Training Grant (GM08572) at the Albert Einstein College of Medicine.

* To whom correspondence should be addressed: Department of Physiology and Biophysics, Albert Einstein College of Medicine of Yeshiva University, Bronx, NY 10461. Telephone: 718-430-4234. Fax: 718-430-4230. E-mail: syeh@aecom.yu.edu.

[1] Abbreviations: hIDO, human recombinant indoleamine 2,3-dioxygenase; iNOS, inducible nitric oxide synthase; NO, nitric oxide; 5C, five coordinate; 6C, six coordinate; IFN-γ, interferon-γ; LPS, lipopolysaccharide; PI, 4-phenylimidazole; CHES, 2-(*N*-cyclohexylamino)ethane sulfonic acid; 3HAA, 3-hydroxyanthranilic acid; NSD, normal-coordinate structural decomposition; Doop, displacement out-of-plane; CO, carbon monoxide; CN, cyanide; DFT, density functional theory; Mb, myoglobin; sGC, soluble guanylate cyclase.

10.1021/bi060143j CCC: $33.50
Published on Web 06/21/2006

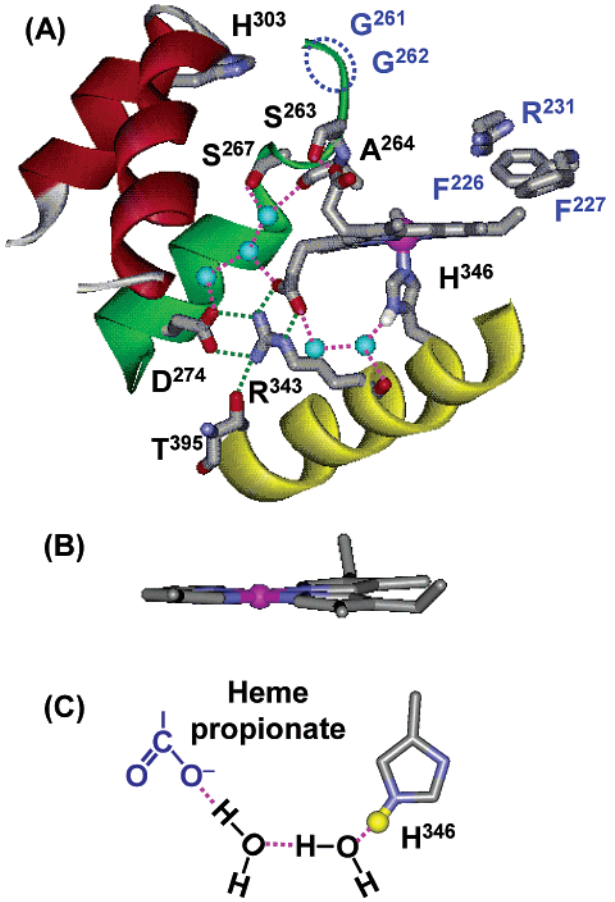

FIGURE 1: (A) Crystallographic structure of hIDO (PDB entry code 2DOT). The proton attached to the nitrogen atom of the proximal histidine (H^{346}) is colored white. The water molecules are labeled as cyan spheres. The hydrogen bonds are shown as dotted lines. The critical residues that may be involved in L-Trp binding are indicated in blue. (B) Distorted porphyrin macrocycle in the ferric derivative of hIDO. For clarity, the methane bridge carbon atoms and the propionate groups are omitted. (C) Hydrogen-bonding network connecting the heme−propionate group and the proximal heme ligand, His^{346}. In this model, the deprotonated propionate group of the heme withdraws the proton (yellow sphere) from the His^{346} through a proton relay pathway, thereby introducing the imidazolate character to it.

to be involved in physiological suppression of airway hyperreactivity in asthma (*22*). It is postulated that IDO limits both pathogen and immune cell proliferation by depleting locally available L-Trp and/or producing cytotoxic metabolites of L-Trp (*23*−*25*).

Recently, the crystal structures of recombinant human IDO (hIDO) were resolved in the 4-phenylimidazole (PI) and cyanide-bound forms (*26*). The overall structure of hIDO is comprised of two distinct domains; each exhibits a unique fold as compared to other known protein structures. The proximal heme-binding pocket is primarily made up of four long α helices from the large domain. The heme iron is coordinated by an evolutionary conserved histidine residue, His^{346}, on the yellow helix shown in Figure 1A, consistent with that predicted by mutagenesis studies and spectroscopic measurements (*27*−*29*). One of the two propionate groups of the heme points toward the distal side of the heme and forms a hydrogen bond with Ser^{263} from the green helix. The other propionate group orients itself toward the proximal side of the heme and is stabilized by an extended hydrogen-bonding network involving the Arg^{343} and Thr^{395} residues from the yellow helix, the Asp^{274}, Ser^{267}, and Ala^{264} residues from the green helix, and several water molecules as indicated in Figure 1A. The mutation of the highly conserved Asp^{274} residue abolishes the heme-binding activity (*27*), suggesting that the hydrogen-bonding network plays an important structural role. The propionate group also forms a unique hydrogen-bonding network with the proximal heme ligand, His^{346}, via two bridging water molecules, as illustrated in Figure 1C. The hydrogen-bonding network introduces imidazolate character to the His^{346}, as suggested by the relatively high frequency of the ν_{Fe-His} mode (236 cm^{-1}) with respect to hemoglobins or myoglobins (*29*).

The distal pocket of the heme is made up of structural elements from each of the two domains and the loop connecting them. Unlike peroxidase or cytochrome P450, no polar residues in the heme distal site were identified as essential for the dioxygenase activity (*26*). Instead, two molecules of 2-(*N*-cyclohexylamino)ethane sulfonic acid (CHES), a component of the crystallization buffer, were found in the heme distal pocket near the iron-bound ligand and the pyrrole ring D of the porphyrin macrocycle and the vinyl group. They locate in the vicinity of the Phe^{226}, Phe^{227}, and Arg^{231} residues and the Gly^{261}/Gly^{262} residue pair in the conserved loop region. Mutagenesis studies suggest that the CHES-binding region coincides with the L-Trp-binding site (*26*), which is indeed consistent with the observations that L-Trp binds in the distal heme pocket and closely interacts with heme iron-bound ligands and that L-Trp binding induces conformational changes to the propionate and vinyl groups of the heme (*29*). Electron paramagnetic resonance spectroscopy along with mutagenesis studies suggest that, in the L-Trp-free hIDO, His^{303} may coordinate to the distal binding site of the heme iron (*30*), accounting for the low-spin contribution to the ferric protein in the absence of L-Trp (*28*, *29*). However, in the crystal structure, the His^{303} residue is located at a remote helix−turn−helix region (labeled as red in Figure 1A), which is isolated from the heme group by the green structural motif. Nonetheless, the highly conserved flexible loop region, AGGSAG for residues 260−265, may facilitate the movement of the green motif, thereby allowing for the coordination of the His^{303} to the heme iron. Clearly, such a large-scale structural movement remains to be confirmed. Although the imidazolate character of the proximal heme ligand, His^{346}, and the distal polar environment introduced by L-Trp binding are both in agreement with a peroxidase-like dioxygen activation mechanism (*29*), the possible structural plasticity and the intriguing hydrogen-bonding networks surrounding the heme group revealed by the new crystallographic data argue that the detailed dioxygenase reaction mechanism may be intricate.

Nitric oxide (NO) is an important regulator of IDO. In the immune system, NO is produced by the inducible isoform of nitric oxide synthase (iNOS), which, like IDO, is induced by IFN-γ and LPS (*31*, *32*). Several lines of regulatory crosstalk have been delineated between iNOS and IDO as illustrated in Scheme 2. For example, one kynurenine pathway metabolite of L-Trp, 3-hydroxyanthranilic acid (3HAA), inhibits iNOS at both the expression and catalytic level (*33*). Another L-Trp metabolite, picolinic acid, acts synergistically with IFN-γ to induce iNOS expression (*34*) (not shown in Scheme 2 for clarity). Conversely, NO produced by iNOS inhibits IDO by preventing its IFN-γ-

Scheme 2: Regulatory Crosstalk between iNOS and IDO

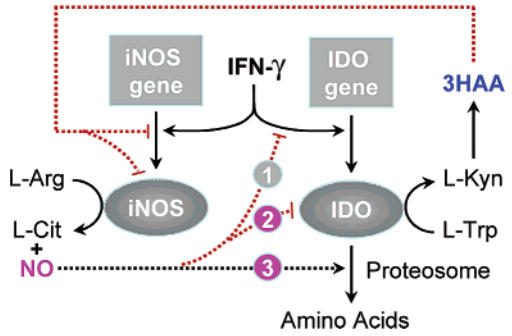

induced expression (*35*) (pathway 1). NO also inhibits the catalytic activity of IDO by interacting with it directly (*35*−*37*) (pathway 2) or by increasing IDO degradation through the proteosome pathway (*38*) (pathway 3). The molecular mechanisms underlying the NO-related inhibition of IDO remain unknown. Previous spectroscopic studies have yielded equivocal results. On the basis of X-ray absorption data (*39*), Aitken and co-workers reported that NO-bound ferrous hIDO is five-coordinate (5C), with a broken proximal Fe−His^{346} bond, but the Soret band was identified at 418 nm, consistent with a six-coordinate (6C) low-spin heme (i.e., the heme iron is coordinated by NO, His^{346}, and four nitrogen atoms of the porphyrin macrocycle) (*28*, *40*).

To further investigate the interactions between NO and hIDO protein (pathways 2 and 3 in Scheme 2), we have initiated a series of optical absorption and resonance Raman spectroscopic studies of the NO adducts of both ferric and ferrous derivatives of hIDO. The effects of pH and oxidation states of the heme and L-Trp on the structural properties of NO-bound hIDO were systematically evaluated. The data will be discussed in the context of the regulatory mechanism of hIDO by NO in vivo.

MATERIALS AND METHODS

The recombinant hIDO protein was prepared on the basis of previously described procedures (*29*). The catalytic activity of hIDO was confirmed by monitoring product (*N*-formylkynurenine) formation with an optical absorbance at 321 nm with an extinction coefficient of 3750 M^{-1} cm^{-1} (*6*). Naturally abundant NO for the Raman measurements was obtained from Tech Air (White Plains, NY), while the isotopically labeled gas, $^{15}N^{16}O$, was supplied by Icon (Summit, NJ). All other materials were purchased from Sigma.

The hIDO samples used were first purged with argon in an anaerobic cell. The NO-bound ferric complexes were formed by injecting 400 μL of 1 atm NO into the sample cell with a Hamilton gastight syringe. To form the NO-bound ferrous complexes, hIDO was first reduced by the injection of argon-purged sodium dithionite, followed by an injection of 400 μL of 1 atm NO. The concentration of the dissolved NO for both the ferric and ferrous samples was estimated to be ∼500 μM based on the volumes of the cell and the sample solution. In the pH titrations with various buffers, potassium phosphate buffer (200 mM) was used for the pH 7.0 and 6.2 preparations, while sodium acetate buffer (200 mM) was used for the pH 5.7, 5.3, 5.0, and 4.6 preparations. For the pH titrations with acetic acid, incremental amounts of argon-purged 10% acetic acid were injected to the hIDO sample in 0.7 M Bis-Tris buffer or a control sample, horse heart myoglobin (Mb), in 0.1 M Bis-Tris buffer. The pH value for each data point was estimated by measuring the pH of the protein-free sample with a pH-meter.

Optical absorption and resonance Raman spectra were taken on instruments described previously (*29*). Briefly, optical absorption spectra were taken on a Shimadzu UV2100U spectrophotometer with a slit width of 1 nm. The resonance Raman spectra were obtained by using 406.7 or 413.1 nm excitation from a Kr ion laser (Spectra Physics, Mountain View, CA). The laser beam was focused to a ∼30 μM spot on the spinning sample cell that rotates during spectral acquisition to avoid photodamage. The typical laser power was 5 mW. The spectral integration times for the pH 7.8 and 4.6 samples were 15−23 and 80 min, respectively. It is important to point out that NO-bound ferric hemeproteins are, in general, prone to autoreduction, especially under laser illumination; as such, the redox state and the integrity of the protein were carefully confirmed here by examining the optical absorption spectra prior to and after each Raman measurement. The NO-dependent vibrational modes were identified by isotope substitution experiments (*29*). The Raman spectra of the $^{15}N^{16}O$-hIDO adducts thus obtained were subtracted from those of the corresponding $^{14}N^{16}O$-hIDO adducts; in the resulting difference spectra, all of the heme vibrational modes were canceled out and the remaining peaks were the modes associated with NO.

To analyze the kinetic as well the pH titration data, optical spectra were fitted with a linear combination of two reference spectra with a program written with MathCad software (Mathsoft, Cambridge, MA). For kinetic measurements, the two reference spectra were obtained from the 6C NO-bound species produced immediately after the addition of NO and the 5C species obtained after equilibrium was reached. For the pH titration experiments, the spectra of the samples at pH 4.6 and 7.0 were used as references. If background scattering in the optical absorption spectrum was significant because of aggregation formation, it was treated as a baseline for the linear analysis. The amount of aggregation formed was estimated by measuring the light scattering at 515 nm, where the absorption extinction coefficients of the 6C and 5C states are minimal and almost equal. The light-scattering data were confirmed by estimating the loss of the soluble protein in the solution.

The out-of-plane displacements of the heme macrocycle of hIDO were calculated from the crystal structures of hIDO (*26*) by using the normal-coordinate structural decomposition (NSD) engine version 2.0, which is available on the Internet (http://jasheln.unm.edu/jasheln/content/nsd/NSDengine/start.htm) (*41*).

RESULTS AND DISCUSSION

NO-Bound Ferric Complex. As a first step to investigate the interactions between NO and hIDO, we measured the optical absorption and resonance Raman spectra of the NO-bound ferric hIDO at pH 7.8. As shown in Figure 2A, the Soret and α/β bands of NO-bound ferric hIDO are identified at 417 and 566/531 nm, respectively, which are very similar to those reported for rabbit IDO (*28*, *40*). The addition of L-Trp to hIDO causes the Soret band to shift to 414 nm, which is accompanied by a slight decrease in the intensity ratio of the α/β bands.

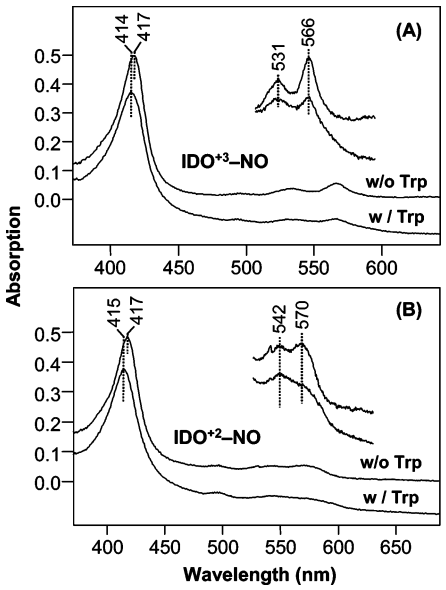

FIGURE 2: Optical absorption spectra of NO-bound ferric (A) and ferrous (B) complexes of hIDO (30 μM) in the absence and presence of 34 mM L-Trp (as indicated) at pH 7.8. The spectra are offset from each other for clarity.

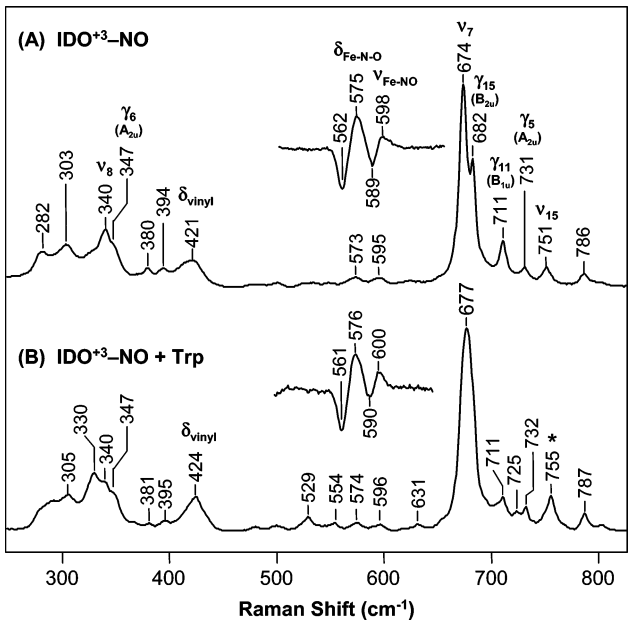

FIGURE 3: Low-frequency resonance Raman spectra of NO-bound ferric complexes of hIDO (30 μM) in the absence (A) and presence (B) of 34 mM L-Trp at pH 7.8 in 50 mM Tris buffer. Isotope difference spectra ($^{14}N^{16}O$ minus $^{15}N^{16}O$) are shown in the insets. The laser excitation wavelength was 413.1 nm. The 755 cm^{-1} band labeled with an asterisk partially originates from tryptophan in free solution as shown in Figure S1 in the Supporting Information.

Figure 3A shows the low-frequency resonance Raman spectrum of the NO-bound ferric hIDO. The low-frequency Raman spectrum of a hemeprotein typically contains iron−ligand stretching/bending modes as well as in-plane and out-of-plane heme deformation modes. In general, the out-of-plane porphyrin modes are Raman-inactive for a planar heme, but they may be activated when the heme adopts an out-of plane geometry because of structural constraints imposed by the surrounding protein matrix (*42*−*44*). The 674, 340, and 751 cm^{-1} bands in Figure 3A are assigned to the in-plane skeletal modes, ν_7, ν_8, and ν_{15}, respectively (*42*). The presence of the out-of-plane heme modes at 731, 711, 682, and 347 cm^{-1} (assigned as γ_5, γ_{11}, γ_{15}, and γ_6, respectively) (*42*, *44*) indicates that the heme group in the NO-bound ferric hIDO adopts an out-of-plane geometry. The out-of-plane deformation of a heme may be quantitatively evaluated with the NSD method developed by Shelnutt et al. (*41*). With this method, the out-of-plane deformation symmetry can be broken down into a linear combination of normal modes, including ruffling (B_{1u}), saddling (B_{2u}), doming (A_{2u}), waving (E_g), and pyrrole-propellering (A_{1u}) deformations. In addition, the out-of-plane displacement along each distortion coordinate can be calculated. A cursory examination of the crystal structures of the 4-phenylimidazole-bound (PDB entry code 2D0T) and cyanide-bound (PDB entry code 2D0U) ferric derivatives of hIDO suggests that the heme is significantly distorted (Figure 1B). With NSD analysis, the total out-of-plane distortion (Doop) of the 4-phenylimidazole-bound hIDO is calculated to be 0.47 and 0.43 Å in the A and B subunits, respectively, as summarized in Table 1. It was also found that the out-of-plane distortion of the heme in hIDO is dominated by the saddling deformation with a B_{2u} symmetry. Similar deformation symmetry was found in the cyanide-bound derivative (Table 1), but the out-of-plane displacement decreases to 0.28 and 0.30 Å for the A and B subunits, respectively, suggesting that the extent of heme deformation is sensitive to the identity of its distal ligand.

Table 1: Out-of-Plane Distortion of the Heme in the 4-Phenylimidazole (PDB Entry Code 2D0T) and Cyanide-Bound (PDB Entry Code 2D0U) Derivatives of hIDO Calculated on the Basis of NSD Analysis

PDB	subunit	Doop	B_{2u}	B_{1u}	A_{2u}	$E_g(x)$	$E_g(y)$	A_{1u}
2D0T	A	0.47	0.47	0.01	0.03	0.03	0.03	0.00
	B	0.43	0.43	0.01	0.06	0.02	0.02	0.02
2D0U	A	0.28	0.28	0.02	0.01	0.01	0.01	0.00
	B	0.30	0.29	0.06	0.03	0.01	0.03	0.01

The presence of the out-of-plane porphyrin modes with A_{2u} (γ_5 and γ_6), B_{1u} (γ_{11}), and B_{2u} (γ_{15}) symmetry types in the L-Trp-free NO-bound ferric hIDO (Figure 3A) suggests that the heme is distorted along these symmetry coordinates. The mixed symmetry type is distinct from that observed in the 4-phenylimidazole- and cyanide-bound derivatives (Table 1), indicating that the out-of-plane distortion is specifically induced by NO binding. Further binding of L-Trp to the protein changes the relative intensities of these out-of-plane modes, the concurrent appearance of new modes at 725, 554, and 529 cm^{-1}, and the broadening of the ν_7 mode (probably because of its upshift in frequency and hence the overlapping with the γ_{15} mode), suggesting changes in the deformation symmetry of the heme macrocycle (*42*, *43*, *45*). The changes in the deformation symmetry of the heme macrocycle in hIDO are associated with the shift of one of the two heme vinyl stretching modes (ν_{vinyl}) from 1631 to 1628 cm^{-1} (Figure S2 in the Supporting Information) and the in-plane vinyl bending mode (δ_{vinyl}) from 421 to 424 cm^{-1} (Figure 3), indicating that L-Trp binding induces a conformational change in one of the two heme vinyl groups. This observation may be accounted for by the fact that Phe^{226}, one of the residues making up the L-Trp-binding site (Figure 1A), is in close proximity to the pyrrole ring D of the porphyrin macrocycle and the vinyl group attached to it. The L-Trp-induced structural perturbation may influence the conjugation

of the π-electron system of the heme, thereby accounting for the altered Soret and α/β transitions shown in Figure 2A.

The Fe−NO stretching (ν_{Fe-NO}) and Fe−N−O bending (δ_{Fe-NO}) modes of hIDO are identified at 598 and 575 cm^{-1}, respectively. They shift to 589 and 562 cm^{-1}, respectively, upon isotope substitution of $^{14}N^{16}O$ with $^{15}N^{16}O$ (inset of Figure 3A). The frequencies of these modes are very similar to those reported for Mb (*46*). Although L-Trp introduces conformational changes to the heme prosthetic group as discussed above, the NO-associated modes are surprisingly insensitive to L-Trp binding (Figure 3B), suggesting that the bound substrate (L-Trp) is not in the vicinity of the Fe−NO moiety. In contrast, the ligand-associated Raman modes in the CO-bound ferrous derivative or CN^--bound ferric derivative are significantly perturbed by L-Trp binding, indicating the close proximity between the heme-bound ligands and the L-Trp (*29*). Furthermore, the out-of-plane distortion of the heme group in the CO- or CN^--bound state is not immediately obvious (if there is any), and L-Trp binding does not disturb its conformation, although L-Trp binding does cause an upshift of both the δ_{vinyl} and ν_{vinyl} (*29*), similar to that found in the NO-bound derivative. On the basis of these observations, we hypothesize that the insensitivity of the Fe−N−O moiety to L-Trp in the NO-bound hIDO is a result of the unique out-of-plane deformation symmetry of the heme, which forces L-Trp to be situated distant from the heme-bound NO.

NO-binding-induced heme distortion has been observed in a NO-transport protein, nitrophorin (*47*), and a NO-producing protein, iNOS (*44*). In both cases, the out-of-plane deformation of the heme has been proposed to retard heme reduction, which is important for their physiological functions. Intriguingly, a recent paper by Papadopoulou et al. reported that the reduction potential of hIDO increases upon L-Trp binding (*30*); our data are hence consistent with the possibility that the increase in the reduction potential is a consequence of the alteration in the heme deformation symmetry. The implication of the nonplanar heme in hIDO certainly warrants further investigation.

NO-Bound Ferrous Complex. The Soret and α/β bands of the NO-bound ferrous hIDO are identified at 417 and 570/542 nm, respectively (Figure 2B), again similar to those reported for the rabbit IDO (*28*, *40*). L-Trp binding induces a shift in the Soret band to 415 nm, which is concomitant with a decrease in the intensity ratio of the α/β band. Parts A and B of Figure 4 shows the low-frequency resonance Raman spectra of the NO-bound ferrous hIDO in the absence and presence of L-Trp, respectively. In the L-Trp-free hIDO, two isotope-sensitive modes are identified at 572 and 595 cm^{-1} (550 and 586 cm^{-1}, respectively, for $^{15}N^{16}O$). Upon L-Trp binding, a new band appears at 463 cm^{-1} (453 cm^{-1} for $^{15}N^{16}O$), which is accompanied by a slight upshift of the 572 cm^{-1} mode to 579 cm^{-1} (562 cm^{-1} for $^{15}N^{16}O$) and a loss of the 595 cm^{-1} mode. The assignments of these NO-related vibrational modes are somewhat ambiguous because of the bent nature of the Fe−N−O moiety in the ferrous protein. In NO-bound ferrous Mb, two modes at 452 and 560 cm^{-1} had been reported as δ_{Fe-N-O} and ν_{Fe-NO}, respectively, by several research groups (*46*, *48*). However, recently, these assignments were questioned by Zeng et al. (*49*). Using nuclear resonance vibrational spectroscopy, the

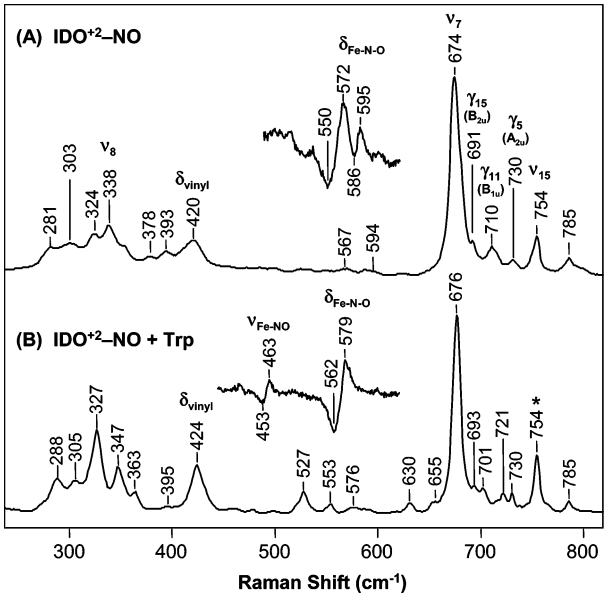

FIGURE 4: Low-frequency resonance Raman spectra of NO-bound ferrous complexes of hIDO (30 μM) in the absence (A) and presence (B) of 34 mM L-Trp at pH 7.8 in 50 mM (B) or 200 mM (A) Tris buffer. Isotope difference spectra ($^{14}N^{16}O$ minus $^{15}N^{16}O$) are shown in the insets. The laser excitation wavelength was 413.1 nm. The 755 cm^{-1} band labeled with an asterisk partially originates from tryptophan in free solution as shown in Figure S1 in the Supporting Information.

authors concluded that the two modes were in fact ν_{Fe-NO} and δ_{Fe-N-O}, respectively, opposite to the conventional view. Although density functional theory (DFT) calculations carried out by Spiro and co-workers suggested that there may be mixing of the two modes (*50*), here, we tentatively assign the 463 and 579 cm^{-1} modes to ν_{Fe-NO} and δ_{Fe-N-O}, respectively, on the basis of the assignment of Zeng et al. (*49*). Likewise, the 572 and 595 cm^{-1} modes present in the L-Trp-free hIDO are assigned to the δ_{Fe-N-O} modes of the two conformers of hIDO.

The absence of the ν_{Fe-NO} mode and presence of the two δ_{Fe-N-O} modes at unusually high frequencies (~12 and 35 cm^{-1} higher than Mb) in the L-Trp-free hIDO indicate an atypical distal heme environment and reflect the unique plasticity of the protein matrix. These structural characteristics may play an important role in driving the proximal heme iron−His bond cleavage reaction and the associated protein conformational changes as will be discussed in the following sections. The two new ν_{Fe-NO} and δ_{Fe-N-O} modes observed in the presence of L-Trp are ~11 and 19 cm^{-1} higher than those reported for Mb as well as other heme protein systems (*46*, *51*, *52*), implying that L-Trp binding induces the protein to convert to a new structure and that L-Trp is in close proximity to the heme-bound NO, in sharp contrast to that in the ferric NO derivative. In general, the Fe^{3+}−N−O moiety in heme proteins assumes a linear geometry, while the Fe^{2+}−N−O moiety prefers a bent conformation (*50*). The sensitivity of the Fe−N−O moiety to L-Trp binding in the ferrous derivative of hIDO but not the ferric derivative argues that the Fe−N−O moiety may bend toward L-Trp, thereby forcing it to interact with L-Trp. This observation suggests that the Fe−O−O moiety in the active form of hIDO may interact with L-Trp in a similar fashion (because it also prefers a bent geometry) and this

interaction may be essential for oxygen insertion to L-Trp during the enzymatic reaction of hIDO.

The data shown in Figure 4A reveal that the heme group in the NO-bound ferrous hIDO is significantly distorted, similar to the ferric derivative (Figure 3A), as evident by the presence of several out-of-plane porphyrin modes, such as γ_5, γ_{11}, and γ_{15} (with A_{2u}, B_{1u}, and B_{2u} symmetry types, respectively). The differences in the relative intensities of these modes in the ferrous form versus the ferric derivative suggest that the deformation symmetries of the ferric and ferrous heme groups are not identical. Akin to the ferric species, L-Trp binding alters the deformation symmetry of the heme macrocycle and the geometry of the vinyl group (as evident by the changes in the δ_{vinyl} and ν_{vinyl} modes shown in Figure 4 and Figure S2 in the Supporting Information, respectively). Intriguingly, the shift of the δ_{vinyl} from 420 to 424 cm^{-1} observed here is very similar to those present in the NO-bound ferric derivative (Figure 3), the CO-bound ferrous derivative (*29*), and the cyanide-bound ferric derivative (*29*), consistent with the view that L-Trp binds in the vicinity of the vinyl group attached to the pyrrole ring D of the porphyrin macrocycle (Figure 1A). The structural change induced by L-Trp binding, like the ferric derivative, may account for the perturbed Soret and α/β transitions shown in Figure 2B and at the same time provide a structural explanation for the inhibitory effect of L-Trp on the proximal Fe−His bond cleavage reaction of NO−hIDO (vide infra).

pH Effects on the NO-Bound Ferrous Complex. During the sample preparation, we found that the structure of the NO-bound ferrous hIDO is very sensitive to small fluctuations in pH. To investigate the pH effect, we first examined the acidic form of hIDO at pH 4.6 with optical absorption as well as resonance Raman spectroscopies. We found that the optical absorption spectrum of the ferrous deoxy derivative of hIDO at pH 4.6 is very similar to that at neutral conditions (data not shown). Upon the addition of 400 μL of 1 atm NO (dissolved [NO] ~500 μM), rapid changes in the optical absorption spectrum were observed (Figure 5A). At the first observable time point (~1 min), the spectrum exhibits a Soret maximum at 415 nm with a pronounced shoulder on the low wavelength side of the peak. Over the next 15 min, the spectrum develops a Soret maximum at 394 nm, with a concomitant decrease in the intensity at 415 nm. The rate of this transition is ascertained by linear analysis of the time-dependent spectra by using the first and last spectra as the references. One typical example of the linear analysis is shown in Figure 5B; the negligible residuals between the data and the simulated spectrum demonstrate the reliability of the process. The resulting populations of the 394 nm species are plotted as a function of time in the inset of Figure 5A. The kinetic trace thus derived is fitted with a single-exponential function with a time constant of 3 min.

The 394 nm optical transition is typical of a 5C NO-bound ferrous heme, as that found in several other hemeproteins, such as soluble guanylate cyclase (sGC) (*53*), cytochrome c' (*54*), cystathione β-synthase (*55*), CooA (*56*), heme-regulated inhibitor (HRI) (*57*), and the acidic form of Mb (*58*). To confirm this assignment, low-frequency resonance Raman spectrum of the 394 nm species was obtained. As shown in Figure 6A, the intensified 348, 678, and 755 cm^{-1} modes, along with the overall spectral pattern, are very

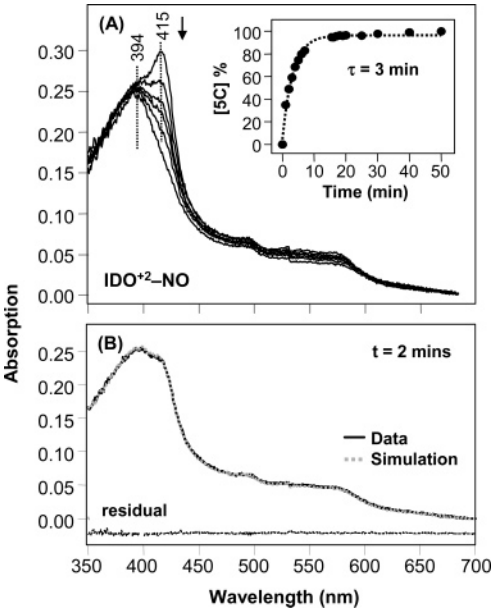

FIGURE 5: (A) Time-dependent spectra obtained following the addition of NO to the ferrous complex of hIDO at pH 4.6. The progression of the spectra is indicated by the arrow. The initial spectrum was taken ~1 min after the addition of NO. The inset shows the kinetic trace of the 5C high-spin species obtained by linear analysis of the time-dependent spectra. The dotted line shows the best single-exponential fit of the kinetic trace with a time constant of 3 min. (B) Typical example for the linear analysis of the time-dependent spectra obtained at $t = 2$ min. The thick solid line and the dotted line are the experimentally observed data and the simulated spectrum, respectively. The difference between the data and the simulated spectrum is shown at the bottom as indicated.

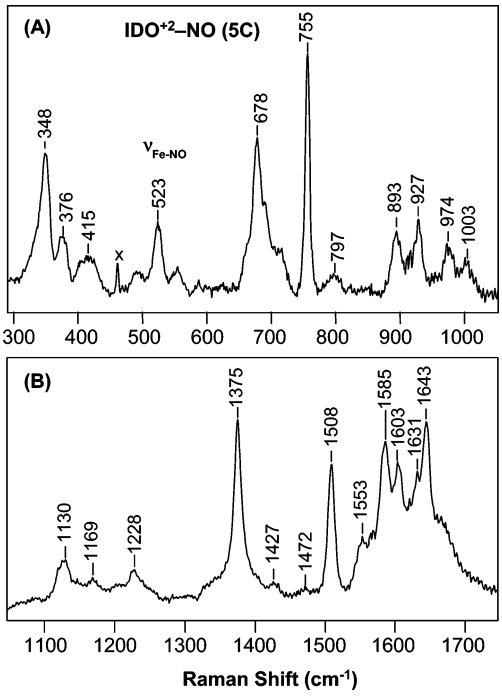

FIGURE 6: Low-frequency (A) and high-frequency (B) regions of the resonance Raman spectrum of the NO-bound 5C high-spin derivative of hIDO (30 μM) at pH 4.6. The laser excitation wavelength was 406.7 nm.

similar to those found in the 5C form of the NO-bound ferrous sGC and Mb (*46*, *59*, *60*). In addition, the Fe−NO stretching mode identified at 523 cm^{-1} is identical to that reported for sGC and Mb. To further confirm that the 394

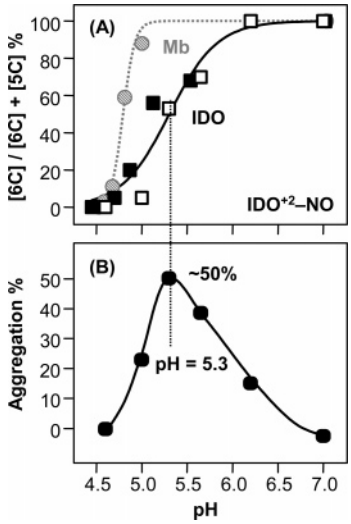

FIGURE 7: (A) Acid titration of $hIDO^{2+}$−NO (30 μM) with a series of buffers (□) or acetic acid (■). As a control, Mb^{2+}−NO was titrated with acetic acid (●). The data were fitted with sigmoidal curves to guide the eyes. (B) Amount of aggregation formation in hIDO as a function of pH generated during the pH titration shown in A.

nm species is indeed a 5C NO-bound ferrous species, the high-frequency resonance Raman spectrum was obtained. Again, the overall spectral pattern (Figure 6B) is nearly identical to that of the NO-bound 5C form of other hemeprotein systems. When these data are taken together, they demonstrate that NO binding to hIDO at pH 4.6 results in the breakage of the proximal Fe−His bond that leads to a NO-bound 5C heme species.

To systematically evaluate the pH effect, we titrated the NO-bound ferrous hIDO with a series of buffers from pH 7.0 to 4.4 (see the Materials and Methods). At each pH, the sample was allowed to incubate for 1 h to ensure that the reaction reached completion. At pH 7.0, 100% of the 6C NO-bound species was observed. As the pH decreases, the population of the 5C species increases until it reaches 100% at pH 4.4. It is important to note that a significant amount of protein aggregation was observed at medium−low pH values. As quantitized by light scattering at 515 nm (see the Materials and Methods), the amount of aggregation follows a bell-shape curve as a function of pH with a maximum at pH 5.3, at which point ~50% of the protein forms aggregation. To examine the mechanism underlying the 6C → 5C transition, each spectrum of the soluble protein at a given pH was fitted with a linear combination of the 6C and 5C spectra. If background scattering in the optical absorption spectrum was significant because of aggregation formation, it was treated as a baseline for the linear analysis. The resulting population of the 6C species is plotted as a function of pH in Figure 7A, which exhibits a transition midpoint of pH 5.3. Intriguingly, the transition midpoint for the 6C → 5C conversion matches the maximum population point of the aggregation, suggesting that the aggregates are derived from an intermediate state positioned between the 6C and 5C states along the reaction coordinate as will be discussed below. Similar pH titration experiments were carried out by adding appropriate amounts of acetic acid to the protein solutions as described in the Materials and Methods. Comparable results were obtained, as shown in Figure 7A, confirming the reliability of the titration data.

Scheme 3: Proposed Reaction Scheme for the NO-Induced Reaction of hIDO and the Associated Potential Energy Diagram

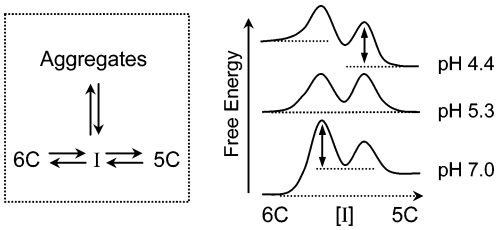

To test if the aggregation formation is a reversible process, we jumped the pH 5.3 sample back to neutral pH by adding incremental amounts of NaOH. It was found that the aggregation can be fully converted to the soluble 5C form but not the 6C state, although 100% of 6C was expected at pH 7.0 on the basis of the data shown in Figure 7A. Likewise, the 5C derivative cannot be reverted back to the 6C form by jumping the pH from 4.6 to 7.0. The inability for the aggregates and 5C to convert to 6C suggests a high-energy barrier separating the aggregation and 5C states from the 6C at neutral pH. When these data are taken together, they suggest a reaction scheme as illustrated in the left panel of Scheme 3. In this model, lowering pH first induces the conversion of the 6C species to an intermediate form (I), which either further transforms to the 5C species or forms aggregates that precipitate out of the solution. The relative energetics of 6C, I, 5C, and aggregates are pH-sensitive as illustrated by the free-energy curves shown in the right panel of Scheme 3 (for clarity, the aggregation state derived from I is not shown). At pH 7.0, 6C is the lowest energy state, because it is the only species populated; in addition, the activation energy barrier for the I → 6C transition is very high because the aggregates and 5C preformed at acidic pH cannot be converted to 6C at neutral pH. At the transition midpoint (pH 5.3), 6C and 5C are isoenergetic because 6C and 5C are equally populated (Figure 7A); in addition, I is higher in energy than the 6C, 5C, and aggregation states because I is not populated at a detectable level. At pH 4.4, 5C (the only species populated) is the lowest energy state; furthermore, the energy barrier for the 6C → I transition is higher than that of the I → 5C transition, as suggested by the two-state kinetic behavior shown in Figure 5A for the 6C → 5C transition.

We hypothesize that the 6C → I transition is associated with protein conformational changes that lead to the exposure of buried hydrophobic groups in hIDO to the solvent, thereby enhancing the propensity for protein aggregation; moreover, the I → 5C transition is associated with an additional structural transition that reburies at least part of the exposed hydrophobic groups, thereby converting the protein to a new soluble form. To further understand the conformational changes in NO−hIDO, we compared its pH-induced structural transition to that of NO-bound ferrous Mb. Similar to NO−hIDO, low pH conditions induce the breakage of the proximal Fe−His bond in NO−Mb and hence the formation of the 5C species. The populations of the 6C derivative were obtained by linear analysis as described above and are plotted as a function of pH in Figure 7A. The transition midpoint of NO−Mb determined here (pH 4.8) is almost identical to that reported in the literature (*58*) and is lower than that of NO−hIDO, despite the fact that the proximal Fe−His bond

is stronger in hIDO as compared to Mb (the ν_{Fe-His} for hIDO and Mb are 236 and 220 cm^{-1}, respectively) (*29*, *61*). In NO−Mb, the 6C → 5C transition curve appears to be much sharper (Figure 7A). It is believed to be initiated by the protonation of the proximal His, and a total of six protons with similar pK_a values are involved (*58*). Because the 6C → 5C transition in NO−Mb is fully reversible and no aggregation was observed, we hypothesize that the broader transition curve of NO−hIDO is a result of the protonation of a collection of protonatable amino acid side chains with differing pK_a values and it is the protonation of these side chain groups that catalyzes the conformational changes associated with the 6C → 5C conversion in NO−hIDO. However, the possibility of the involvement of a smaller number of protons in hIDO as compared to that of NO−Mb cannot be excluded at present.

The conformational changes associated with the NO-induced 6C → 5C transition presented here for hIDO are not unprecedented. It has been demonstrated in the α chain of human hemoglobin (*62*) and in another important heme-protein, sGC, which is linked to a cascade of signal transduction pathways in vivo (*63*). On the other hand, although protein aggregates are typically considered as nonphysiologically important byproducts of native functional proteins, recently, the important roles of aggregated proteins have begun to be unveiled in several important biological systems. They have been implicated in neurodegenerative diseases, such as Huntington's, Parkinson's, Alzheimer's, and prion diseases, as the toxic materials that cause diseases (*64*). In contrast, yeast prion aggregates produce heritable changes in the phenotype that are beneficial for the organism (*65*). Likewise, a prion-like state of a neuronal isoform of CPEB (cytoplasmic polyadenylation element-binding protein) has been suggested to help maintain long-term synaptic changes associated with memory storage (*66*). Considering these new findings, a functional role of the aggregation state of NO−hIDO certainly cannot be ruled out.

pH Effects on the NO-Bound Ferric Complex. To investigate if the oxidation state of the heme iron affects the pH-induced structural changes, the reaction of the ferric hIDO following the addition of 400 μL of 1 atm NO (dissolved [NO] ∼500 μM) at pH 4.6 was monitored by optical absorption spectroscopy. In contrast to the ferrous protein, within the deadtime of our measurements (∼1 min), a Soret band at 417 nm and α/β bands at 566/530 nm, typical for a 6C NO-bound ferric heme protein, were observed (Figure 8A), indicating that the NO-binding reaction to the ferric protein is completed within ∼1 min. The 6C NO-bound ferric species gradually converts to a 394 nm species, which is almost identical to the NO-bound 5C ferrous hIDO shown in Figure 5A. Resonance Raman spectroscopic studies of the 394 nm species confirm that it is indeed a 5C NO-bound ferrous hIDO (see Figure S3 in the Supporting Information). The conversion from the 6C NO-bound ferric state to the 5C NO-bound ferrous state exhibits a clear isosbestic point at 399 nm, reflecting a two-state-like structural transition. Each time-resolved spectrum can be fitted with a linear combination of the first and last spectrum with satisfactory residuals. The population of the 5C species thus obtained is plotted as a function of the reaction time in the inset of Figure 8A. The resulting kinetic trace is fitted with a single-exponential function with a time constant of 64 min. On the basis of these observations, we propose the following sequential model:

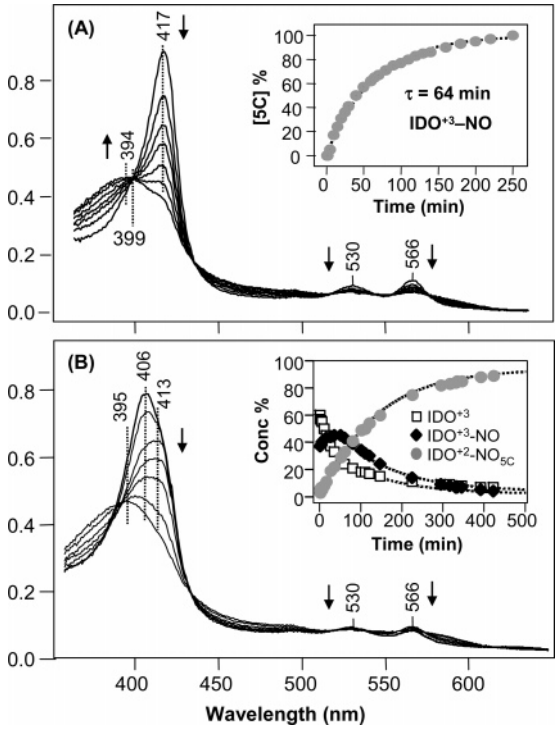

FIGURE 8: Time-dependent spectra obtained following the addition of (A) 400 μL and (B) 50 μL of 1 atm NO to the ferric complex of hIDO at pH 4.6. The progression of the spectra is indicated by the arrows. The initial spectrum was taken ∼1 min after the addition of NO. The inset in A shows the kinetic trace of the 5C NO-bound ferrous species obtained by linear analysis of the time-resolved spectra; the dotted line shows the best single-exponential fit of the kinetic trace with a time constant of 64 min. The inset in B shows the kinetic traces of the 6C NO-free ferric species (IDO^{3+}), 6C NO-bound ferric species ($IDO^{3+}-NO$), and 5C NO-bound ferrous species ($IDO^{2+}-NO_{5C}$) obtained by linear analysis of the time-resolved spectra; the dotted lines show the best fit of the kinetic traces.

$$hIDO^{3+}-NO\ (6C) \xrightarrow{k_1} [hIDO^{2+}-NO\ (6C)] \xrightarrow{k_2} hIDO^{2+}-NO\ (5C) \quad (1)$$

In this model, the 6C NO-bound ferric hIDO is first autoreduced by NO to generate 6C NO-bound ferrous hIDO with a rate constant of k_1. The reaction is followed by the breakage of the proximal Fe−His bond, thereby leading to the 5C NO-bound species, an identical reaction as that shown in Figure 5A (hence, $1/k_2 \sim 3$ min). The 6C NO-bound ferrous species shown in the bracket does not accumulate to a detectable level, because the reaction is rate-limited by the autoreduction process (i.e., $1/k_2 \sim 1/k_{obs} \sim 64$ min).

Autoreduction of the NO-bound ferric heme has been reported in several hemeprotein systems. Although the detail mechanism remains unclear, it is the general consensus that the electron source for the reduction is from NO molecule-(s) (*67*−*70*). To test this proposal in hIDO, we reduced the amount of NO injected into the reaction mixture by a factor of 8 and followed the same reaction as a function of time. As shown in Figure 8B, the Soret maximum first red-shifts from 406 to ∼413 nm (Figure 8B), reflecting NO binding to the ferric protein, and subsequently blue-shifts to 395 nm, indicating the same autoreduction and Fe−His bond breakage

reaction as that shown in Figure 8A and illustrated in eq 1. It is noted that the Soret maximum does not shift all of the way to 417 nm, a wavelength expected for the NO-bound ferric derivative, because it is not populated to an appreciable level during the reaction. Linear analysis of the time-resolved spectra with the standard spectra of $hIDO^{3+}$, $hIDO^{3+}-NO$ (6C), and $hIDO^{2+}-NO$ (5C) results in the kinetic traces shown in the inset of Figure 8B. The kinetic traces are fitted with a three-state sequential model: $hIDO^{3+} \rightarrow hIDO^{3+}-NO$ (6C) $\rightarrow hIDO^{2+}-NO$ (5C). The rates for the first and second steps are estimated to be 56 and 150 min^{-1}, respectively. The best-fitted kinetic curves are shown as the dotted lines in the inset of Figure 8B. The reduction of the rate for the $hIDO^{3+}-NO$ (6C) $\rightarrow hIDO^{2+}-NO$ (5C) transition in response to the decrease in the NO concentration confirms that the electron source for the autoredution process is NO. The prerequisite for NO−hIDO to be reduced prior to the bond-breakage reaction suggests that the redox state of the heme, in addition to the abundance of NO, is an important factor for the regulation of hIDO activity in vivo.

Effects of L*-Trp on the pH-Induced Structural Change.* To test if L-Trp binding affects the NO-induced proximal iron−His bond cleavage reaction in hIDO, the same pH-induced reactions shown in Figures 5A and 8A were tested in the presence of L-Trp. To our surprise, the addition of L-Trp totally inhibits the 6C → 5C transition in both the ferric and ferrous states, although in the case of the NO-bound ferric hIDO, acidic pH seems to induce partial denaturation of the protein matrix as indicated by the noticeable release of heme into free solution. Although it is unclear exactly how binding L-Trp to the distal side of the heme affects the stability of the proximal heme Fe−His bond, resonance Raman data shown in Figure 4 suggest that a direct interaction between L-Trp and the peripheral groups of the heme and the associated changes in the deformation symmetry of the heme macrocycle and the surrounding protein matrix may be responsible for the stabilization of the proximal Fe−His bond.

CONCLUSIONS

On the basis of the spectroscopic studies reported here, the heme macrocycle in the NO-bound ferrous derivative of hIDO adopts an out-of-plane structure and the heme and its bound exogenous ligand (NO) are located in an unusual protein environment that is sensitive to the binding of the substrate, L-Trp. A small decrease in pH from neutrality induces the rupture of the proximal heme iron−His bond, which leads to the formation of a 5C NO-bound derivative. We hypothesize that the unexpected lability of the Fe−His bond discovered here accounts for the discrepancy between the optical absorption and X-ray absorption data reported by Aitken et al. (*39*), because the high-energy X-ray beam may introduce a small structural perturbation to hIDO, thereby weakening the Fe−His bond. We have demonstrated that the proximal iron−His bond cleavage reaction is associated with protein conformational changes, which may provide a molecular mechanism that accounts for the increased degradation of hIDO in vivo induced by NO (*38*). Hucke et al. reported that NO increased hIDO degradation in the proteosome over a period of 16 h (*38*). For a protein to enter the proteosome degradation pathway, it must first expose a normally buried conformational motif or amino acid sequence that is recognized by ubiquitin ligase as a degradation signal. We postulate that the cleavage of the proximal Fe−His bond induced by NO changes the deformation symmetry of the heme macrocycle, which subsequently induces conformational changes to the protein matrix, thereby exposing the degradation signal to the ubiquitin ligase system. It is important to point out that NO-induced protein conformational changes have been demonstrated in another important hemeprotein, sGC, which potentiates a cascade of signal transduction pathways in vivo (*63*). Intriguingly, the bond cleavage of sGC occurs at neural pH, whereas that of hIDO only takes place when the pH slightly departs from neutrality (pH <6.5), and it is fully inhibited by the substrate, L-Trp.

It remains uncertain if the NO-inactivation mechanism of hIDO can be modulated by pH and L-Trp in vivo as implied by this work, because the local pH and L-Trp concentration under (patho)physiological conditions are not available in the literature; nonetheless, two previously proposed scenarios do support their physiological significance. First, the activity and expression of IDO in tumor cells have been linked to tumoral immune resistance (*20*), plausibly because of the depletion of L-Trp that is essential for immune cell proliferation (*23*). This hypothesis is supported by a recent discovery that an hIDO inhibitor was found to potentiate the effects of chemotherapeutic agents on tumor regression (*21*). Historically, the intracellular environment of cancer cells was thought to be acidic because of an increased production of lactic acid (*71, 72*). More current work, however, indicates that the cytosolic pH of tumor cells is not acidic (*73*), despite an acidic extracellular environment (*74*). Nevertheless, a breakdown in the intracellular pH homeostasis may be responsible for the immune-linked spontaneous regression of some malignant tumors (see refs *75* and *76* and references therein). It is plausible that a breakdown in the pH homeostatic mechanisms in cancer cells causes a slight decrease in pH that leads to the reduction in hIDO activity and increase in hIDO degradation, thereby reducing immune tolerance to cancer and facilitating immune mobilization against cancer cells. Second, Thomas and Stocker proposed a sequential antimicrobial defense mechanism for the immune response, in which hIDO activity is a first-line of defense against invading pathogens, whereas iNOS activity is a component of a later-line defense against persistent infection (*77*). In view of the facts that IDO activity has been linked to immune tolerance and that one of the metabolites of hIDO inhibits iNOS at both the expression and catalytic level (*33*), it is important that hIDO activity is repressed efficiently by NO produced by iNOS and it is reasonable to hypothesize that the NO-inhibition efficiency is optimized during the transition from the hIDO-related defense phase to the iNOS-associated defense phase, when the L-Trp concentration is most likely at its lowest point. Conversely, when the cellular level of L-Trp is relatively high, it may be essential to maintain the activity of hIDO by preventing NO inactivation of hIDO. Hence, it would appear logical that the NO-induced inactivation of hIDO can be inhibited by L-Trp.

In summary, although NO can inhibit hIDO by directly binding to the heme iron, its further conversion to the 5C species provides a sound mechanism to account for the well-timed and efficient NO inhibition required for the immune response. It accounts for the inhibition mechanism of hIDO

by NO produced by the immune system that allows for the sequential execution of hIDO and iNOS activity in pathogen and tumor clearance processes and the spontaneous regression of tumor cells failing to control their cellular pH environment. Our data suggest that the NO-dependent regulatory mechanisms of hIDO can be modulated by several cellular factors, including pH, redox environment, and NO and L-Trp abundance. Considering the complexity of the immune system, these extra points of regulation may be indispensable for guaranteeing that hIDO activity is accurately controlled. Exactly how these factors affect hIDO activity in a synergetic fashion under physiological conditions is certainly worthy of further investigation.

ACKNOWLEDGMENT

We thank Dr. Denis L. Rousseau and Dr. John Chan for valuable discussions and Mr. Yinghua Wang for expressing and purifying the protein samples.

SUPPORTING INFORMATION AVAILABLE

Raman spectrum of trptophan in water, the high-frequency resonance Raman spectra of the 6C NO-bound ferric and ferrous derivatives of hIDO, and the resonance Raman spectra of the 5C NO-bound ferrous derivative of hIDO produced by the addition of NO to the ferric enzyme at pH 4.6. This material is available free of charge via the Internet at http://pubs.acs.org.

REFERENCES

1. Tone, S., Takikawa, O., Habara-Ohkubo, A., Kadoya, A., Yoshida, R., and Kido, R. (1990) Primary structure of human indoleamine 2,3-dioxygenase deduced from the nucleotide sequence of its cDNA, *Nucleic Acids Res. 18*, 367.
2. Yamamoto, S., and Hayaishi, O. (1967) Tryptophan pyrrolase of rabbit intestine. D- and L-tryptophan-cleaving enzyme or enzymes, *J. Biol. Chem. 242*, 5260−5266.
3. Hayaishi, O., Hirata, F., Ohnishi, T., Henry, J. P., Rosenthal, I., and Katoh, A. (1977) Indoleamine 2,3-dioxygenase: Incorporation of $^{18}O_2^-$ and $^{18}O_2$ into the reaction products, *J. Biol. Chem. 252*, 3548−3550.
4. Taniguchi, T., Sono, M., Hirata, F., Hayaishi, O., Tamura, M., Hayashi, K., Iizuka, T., and Ishimura, Y. (1979) Indoleamine 2,3-dioxygenase. Kinetic studies on the binding of superoxide anion and molecular oxygen to enzyme, *J. Biol. Chem. 254*, 3288−3294.
5. Sono, M., Roach, M. P., Coulter, E. D., and Dawson, J. H. (1996) Heme-containing oxygenases, *Chem. Rev. 96*, 2841−2888.
6. Shimizu, T., Nomiyama, S., Hirata, F., and Hayaishi, O. (1978) Indoleamine 2,3-dioxygenase. Purification and some properties, *J. Biol. Chem. 253*, 4700−4706.
7. Hirata, F., Hayaishi, O., Tokuyama, T., and Seno, S. (1974) In vitro and in vivo formation of two new metabolites of melatonin, *J. Biol. Chem. 249*, 1311−1313.
8. Hood, B. D., Garner, B., and Truscott, R. J. (1999) Human lens coloration and aging. Evidence for crystallin modification by the major ultraviolet filter, 3-hydroxy-kynurenine *O*-*β*-D-glucoside, *J. Biol. Chem. 274*, 32547−32550.
9. Vazquez, S., Aquilina, J. A., Jamie, J. F., Sheil, M. M., and Truscott, R. J. (2002) Novel protein modification by kynurenine in human lenses, *J. Biol. Chem. 277*, 4867−4873.
10. Yoshida, R., Imanishi, J., Oku, T., Kishida, T., and Hayaishi, O. (1981) Induction of pulmonary indoleamine 2,3-dioxygenase by interferon, *Proc. Natl. Acad. Sci. U.S.A. 78*, 129−132.
11. Yoshida, R., and Hayaishi, O. (1978) Induction of pulmonary indoleamine 2,3-dioxygenase by intraperitoneal injection of bacterial lipopolysaccharide, *Proc. Natl. Acad. Sci. U.S.A. 75*, 3998−4000.
12. Pfefferkorn, E. R. (1984) Interferon *γ* blocks the growth of *Toxoplasma gondii* in human fibroblasts by inducing the host cells to degrade tryptophan, *Proc. Natl. Acad. Sci. U.S.A. 81*, 908−912.
13. Daubener, W., Spors, B., Hucke, C., Adam, R., Stins, M., Kim, K. S., and Schroten, H. (2001) Restriction of *Toxoplasma gondii* growth in human brain microvascular endothelial cells by activation of indoleamine 2,3-dioxygenase, *Infect. Immun. 69*, 6527−6531.
14. Mahon, B. P., and Mills, K. H. (1999) Interferon-*γ* mediated immune effector mechanisms against *Bordetella pertussis*, *Immunol. Lett. 68*, 213−217.
15. Bodaghi, B., Goureau, O., Zipeto, D., Laurent, L., Virelizier, J. L., and Michelson, S. (1999) Role of IFN-*γ*-induced indoleamine 2,3-dioxygenase and inducible nitric oxide synthase in the replication of human cytomegalovirus in retinal pigment epithelial cells, *J. Immunol. 162*, 957−964.
16. Schroten, H., Spors, B., Hucke, C., Stins, M., Kim, K. S., Adam, R., and Daubener, W. (2001) Potential role of human brain microvascular endothelial cells in the pathogenesis of brain abscess: Inhibition of *Staphylococcus aureus* by activation of indoleamine 2,3-dioxygenase, *Neuropediatrics 32*, 206−210.
17. Bozza, S., Fallarino, F., Pitzurra, L., Zelante, T., Montagnoli, C., Bellocchio, S., Mosci, P., Vacca, C., Puccetti, P., and Romani, L. (2005) A crucial role for tryptophan catabolism at the host/*Candida albicans* interface, *J. Immunol. 174*, 2910−2918.
18. Obojes, K., Andres, O., Kim, K. S., Daubener, W., and Schneider-Schaulies, J. (2005) Indoleamine 2,3-dioxygenase mediates cell type-specific anti-measles virus activity of *γ* interferon, *J. Virol. 79*, 7768−7776.
19. Munn, D. H., Zhou, M., Attwood, J. T., Bondarev, I., Conway, S. J., Marshall, B., Brown, C., and Mellor, A. L. (1998) Prevention of allogeneic fetal rejection by tryptophan catabolism, *Science 281*, 1191−1193.
20. Uyttenhove, C., Pilotte, L., Theate, I., Stroobant, V., Colau, D., Parmentier, N., Boon, T., and van den Eynde, B. J. (2003) Evidence for a tumoral immune resistance mechanism based on tryptophan degradation by indoleamine 2,3-dioxygenase, *Nat. Med. 9*, 1269−1274.
21. Muller, A. J., DuHadaway, J. B., Donover, P. S., Sutanto-Ward, E., and Prendergast, G. C. (2005) Inhibition of indoleamine 2,3-dioxygenase, an immunoregulatory target of the cancer suppression gene Bin1, potentiates cancer chemotherapy, *Nat. Med. 11*, 312−319.
22. Hayashi, T., Beck, L., Rossetto, C., Gong, X., Takikawa, O., Takabayashi, K., Broide, D. H., Carson, D. A., and Raz, E. (2004) Inhibition of experimental asthma by indoleamine 2,3-dioxygenase, *J. Clin. Invest. 114*, 270−279.
23. Munn, D. H., Shafizadeh, E., Attwood, J. T., Bondarev, I., Pashine, A., and Mellor, A. L. (1999) Inhibition of T cell proliferation by macrophage tryptophan catabolism, *J. Exp. Med. 189*, 1363−1372.
24. Frumento, G., Rotondo, R., Tonetti, M., Damonte, G., Benatti, U., and Ferrara, G. B. (2002) Tryptophan-derived catabolites are responsible for inhibition of T and natural killer cell proliferation induced by indoleamine 2,3-dioxygenase, *J. Exp. Med. 196*, 459−468.
25. Moffett, J. R., and Namboodiri, M. A. (2003) Tryptophan and the immune response, *Immunol. Cell Biol. 81*, 247−265.
26. Sugimoto, H., Oda, S. I., Otsuki, T., Hino, T., Yoshida, T., and Shiro, Y. (2006) Crystal structure of human indoleamine 2,3-dioxygenase: Catalytic mechanism of O_2 incorporation by a heme-containing dioxygenase, *Proc. Natl. Acad. Sci. U.S.A. 103*, 2611−2616.
27. Littlejohn, T. K., Takikawa, O., Truscott, R. J., and Walker, M. J. (2003) Asp274 and His346 are essential for heme binding and catalytic function of human indoleamine 2,3-dioxygenase, *J. Biol. Chem. 278*, 29525−29531.
28. Sono, M., and Dawson, J. H. (1984) Extensive studies of the heme coordination structure of indoleamine 2,3-dioxygenase and of tryptophan binding with magnetic and natural circular dichroism and electron paramagnetic resonance spectroscopy, *Biochim. Biophys. Acta 789*, 170−187.
29. Terentis, A. C., Thomas, S. R., Takikawa, O., Littlejohn, T. K., Truscott, R. J., Armstrong, R. S., Yeh, S. R., and Stocker, R. (2002) The heme environment of recombinant human indoleamine 2,3-dioxygenase. Structural properties and substrate−ligand interactions, *J. Biol. Chem. 277*, 15788−15794.
30. Papadopoulou, N. D., Mewies, M., McLean, K. J., Seward, H. E., Svistunenko, D. A., Munro, A. W., and Raven, E. L. (2005)

Redox and spectroscopic properties of human indoleamine 2,3-dioxygenase and a His303Ala variant: Implications for catalysis, *Biochemistry 44*, 14318−14328.
31. Geller, D. A., and Billiar, T. R. (1998) Molecular biology of nitric oxide synthases, *Cancer Metastasis Rev. 17*, 7−23.
32. Kleinert, H., Schwarz, P. M., and Forstermann, U. (2003) Regulation of the expression of inducible nitric oxide synthase, *Biol. Chem. 384*, 1343−1364.
33. Sekkai, D., Guittet, O., Lemaire, G., Tenu, J. P., and Lepoivre, M. (1997) Inhibition of nitric oxide synthase expression and activity in macrophages by 3-hydroxyanthranilic acid, a tryptophan metabolite, *Arch. Biochem. Biophys. 340*, 117−123.
34. Melillo, G., Cox, G. W., Biragyn, A., Sheffler, L. A., and Varesio, L. (1994) Regulation of nitric-oxide synthase mRNA expression by interferon-γ and picolinic acid, *J. Biol. Chem. 269*, 8128−8133.
35. Alberati-Giani, D., Malherbe, P., Ricciardi-Castagnoli, P., Kohler, C., Denis-Donini, S., and Cesura, A. M. (1997) Differential regulation of indoleamine 2,3-dioxygenase expression by nitric oxide and inflammatory mediators in IFN-γ-activated murine macrophages and microglial cells, *J. Immunol. 159*, 419−426.
36. Thomas, S. R., Mohr, D., and Stocker, R. (1994) Nitric oxide inhibits indoleamine 2,3-dioxygenase activity in interferon-γ primed mononuclear phagocytes, *J. Biol. Chem. 269*, 14457−14464.
37. Daubener, W., Posdziech, V., Hadding, U., and MacKenzie, C. R. (1999) Inducible anti-parasitic effector mechanisms in human uroepithelial cells: Tryptophan degradation vs. NO production, *Med. Microbiol. Immunol. 187*, 143−147.
38. Hucke, C., MacKenzie, C. R., Adjogble, K. D., Takikawa, O., and Daubener, W. (2004) Nitric oxide-mediated regulation of γ interferon-induced bacteriostasis: Inhibition and degradation of human indoleamine 2,3-dioxygenase, *Infect. Immun. 72*, 2723−2730.
39. Aitken, J. B., Thomas, S. E., Stocker, R., Thomas, S. R., Takikawa, O., Armstrong, R. S., and Lay, P. A. (2004) Determination of the nature of the heme environment in nitrosyl indoleamine 2,3-dioxygenase using multiple-scattering analyses of X-ray absorption fine structure, *Biochemistry 43*, 4892−4898.
40. Sono, M. (1986) Spectroscopic and equilibrium properties of the indoleamine 2,3-dioxygenase−tryptophan−O_2 ternary complex and of analogous enzyme derivatives. Tryptophan binding to ferrous enzyme adducts with dioxygen, nitric oxide, and carbon monoxide, *Biochemistry 25*, 6089−6097.
41. Jentzen, W., Ma, J. G., and Shelnutt, J. A. (1998) Conservation of the conformation of the porphyrin macrocycle in hemoproteins, *Biophys. J. 74*, 753−763.
42. Hu, S., Smith, K. M., and Spiro, T. G. (1996) Assignment of protoheme resonance Raman spectrum by heme labeling in myoglobin, *J. Am. Chem. Soc. 118*, 12638−12646.
43. Yeh, S. R., Takahashi, S., Fan, B., and Rousseau, D. L. (1997) Ligand exchange during cytochrome *c* folding, *Nat. Struct. Biol. 4*, 51−56.
44. Li, D., Stuehr, D. J., Yeh, S. R., and Rousseau, D. L. (2004) Heme distortion modulated by ligand−protein interactions in inducible nitric-oxide synthase, *J. Biol. Chem. 279*, 26489−26499.
45. Deng, T. J., Proniewicz, L. M., Kincaid, J. R., Yeom, H., Macdonald, I. D., and Sligar, S. G. (1999) Resonance Raman studies of cytochrome P450 μ_B3 and its complexes with exogenous ligands, *Biochemistry 38*, 13699−13706.
46. Tomita, A., Hirota, S., Ogura, T., Olson, J. S., and Kitagawa, T. (1999) Resonance Raman investigation of Fe−N−O structure of nitrosylheme in myoglobin and its mutants, *J. Phys. Chem. B 103*, 7044−7054.
47. Walker, F. A. (2005) Nitric oxide interaction with insect nitrophorins and thoughts on the electron configuration of the $\{FeNO\}_6$ complex, *J. Inorg. Biochem. 99*, 216−236.
48. Coyle, C. M., Vogel, K. M., Rush, T. S., III, Kozlowski, P. M., Williams, R., Spiro, T. G., Dou, Y., Ikeda-Saito, M., Olson, J. S., and Zgierski, M. Z. (2003) FeNO structure in distal pocket mutants of myoglobin based on resonance Raman spectroscopy, *Biochemistry 42*, 4896−4903.
49. Zeng, W., Silvernail, N. J., Wharton, D. C., Georgiev, G. Y., Leu, B. M., Scheidt, W. R., Zhao, J., Sturhahn, W., Alp, E. E., and Sage, J. T. (2005) Direct probe of iron vibrations elucidates NO activation of heme proteins, *J. Am. Chem. Soc. 127*, 11200−11201.
50. Vogel, K. M., Kozlowski, P. M., Zgierski, M. Z., and Spiro, T. G. (1999) Determinants of the FeXO (X = C, N, O) vibrational frequencies in heme adducts from experiments and density functional theory, *J. Am. Chem. Soc. 121*, 9915−9921.
51. Hu, S., and Kincaid, J. R. (1991) Resonance Raman characterization of nitric oxide adducts of cytochrome P450cam: The effect of substrate structure on the iron-ligand vibrations, *J. Am. Chem. Soc. 113*, 2843−2850.
52. Wang, J., Rousseau, D. L., Abu-Soud, H. M., and Stuehr, D. J. (1994) Heme coordination of NO in NO synthase, *Proc. Natl. Acad. Sci. U.S.A. 91*, 10512−10516.
53. Stone, J. R., and Marletta, M. A. (1994) Soluble guanylate cyclase from bovine lung: Activation with nitric oxide and carbon monoxide and spectral characterization of the ferrous and ferric states, *Biochemistry 33*, 5636−5640.
54. Andrew, C. R., George, S. J., Lawson, D. M., and Eady, R. R. (2002) Six- to five-coordinate heme-nitrosyl conversion in cytochrome *c′* and its relevance to guanylate cyclase, *Biochemistry 41*, 2353−2360.
55. Taoka, S., and Banerjee, R. (2001) Characterization of NO binding to human cystathionine β-synthase: Possible implications of the effects of CO and NO binding to the human enzyme, *J. Inorg. Biochem. 87*, 245−251.
56. Reynolds, M. F., Parks, R. B., Burstyn, J. N., Shelver, D., Thorsteinsson, M. V., Kerby, R. L., Roberts, G. P., Vogel, K. M., and Spiro, T. G. (2000) Electronic absorption, EPR, and resonance Raman spectroscopy of CooA, a CO-sensing transcription activator from *R. rubrum*, reveals a five-coordinate NO−heme, *Biochemistry 39*, 388−396.
57. Igarashi, J., Sato, A., Kitagawa, T., Yoshimura, T., Yamauchi, S., Sagami, I., and Shimizu, T. (2004) Activation of heme-regulated eukaryotic initiation factor 2α kinase by nitric oxide is induced by the formation of a five-coordinate NO−heme complex: Optical absorption, electron spin resonance, and resonance Raman spectral studies, *J. Biol. Chem. 279*, 15752−15762.
58. Duprat, A. F., Traylor, T. G., Wu, G. Z., Coletta, M., Sharma, V. S., Walda, K. N., and Magde, D. (1995) Myoglobin-NO at low pH: Free four-coordinated heme in the protein pocket, *Biochemistry 34*, 2634−2644.
59. Fan, B., Gupta, G., Danziger, R. S., Friedman, J. M., and Rousseau, D. L. (1998) Resonance Raman characterization of soluble guanylate cyclase expressed from baculovirus, *Biochemistry 37*, 1178−1184.
60. Karow, D. S., Pan, D., Tran, R., Pellicena, P., Presley, A., Mathies, R. A., and Marletta, M. A. (2004) Spectroscopic characterization of the soluble guanylate cyclase-like heme domains from *Vibrio cholerae* and *Thermoanaerobacter tengcongensis*, *Biochemistry 43*, 10203−10211.
61. Hirota, S., Mizoguchi, Y., Yamauchi, O., and Kitagawa, T. (2002) Observation of an isotope-sensitive low-frequency Raman band specific to metmyoglobin, *J. Biol. Inorg. Chem. 7*, 217−221.
62. Nagai, K., Welborn, C., Dolphin, D., and Kitagawa, T. (1980) Resonance Raman evidence for cleavage of the Fe−N ϵ(His-F8) bond in the α subunit of the T-structure nitrosylhemoglobin, *Biochemistry 19*, 4755−4761.
63. Denninger, J. W., and Marletta, M. A. (1999) Guanylate cyclase and the NO/cGMP signaling pathway, *Biochim. Biophys. Acta 1411*, 334−350.
64. Selkoe, D. J. (2003) Folding proteins in fatal ways, *Nature 426*, 900−904.
65. Glover, J. R., Kowal, A. S., Schirmer, E. C., Patino, M. M., Liu, J. J., and Lindquist, S. (1997) Self-seeded fibers formed by Sup35, the protein determinant of $[PSI^+]$, a heritable prion-like factor of *S. cerevisiae*, *Cell 89*, 811−819.
66. Si, K., Lindquist, S., and Kandel, E. R. (2003) A neuronal isoform of the aplysia CPEB has prion-like properties, *Cell 115*, 879−891.
67. Keilin, D., and Hartree, E. F. (1937) Reaction of nitric oxide with haemoglobin and methaemoglobin, *Nature 139*, 548.
68. Chien, J. C. (1969) Reactions of nitric oxide with methemoglobin, *J. Am. Chem. Soc. 91*, 2166−2168.
69. Addison, A. W., and Stephanos, J. J. (1986) Nitrosyliron(III) hemoglobin: Autoreduction and spectroscopy, *Biochemistry 25*, 4104−4113.
70. Boffi, A., Sarti, P., Amiconi, G., and Chiancone, E. (2002) The interplay between heme iron and protein sulfhydryls in the reaction of dimeric *Scapharca inaequivalvis* hemoglobin with nitric oxide, *Biophys. Chem. 98*, 209−216.

71. Warburg, O. (1956) On the origin of cancer cells, *Science 123*, 309−314.
72. Simon, S. M., and Schindler, M. (1994) Cell biological mechanisms of multidrug resistance in tumors, *Proc. Natl. Acad. Sci. U.S.A. 91*, 3497−3504.
73. Stubbs, M., Veech, R. L., and Griffiths, J. R. (1995) Tumor metabolism: The lessons of magnetic resonance spectroscopy, *Adv. Enzyme Regul. 35*, 101−115.
74. Shrode, L. D., Tapper, H., and Grinstein, S. (1997) Role of intracellular pH in proliferation, transformation, and apoptosis, *J. Bioenerg. Biomembr. 29*, 393−399.
75. Harguindey, S. (1982) Hydrogen ion dynamics and cancer: An appraisal, *Med. Pediatr. Oncol. 10*, 217−236.
76. Harguindey, S., and Cragoe, E. J., Jr. (1992) The Na^+/H^+ antiporter in oncology in the light of the spontaneous regression of cancer and cell metabolism, *Med. Hypotheses 39*, 229−237.
77. Thomas, S. R., and Stocker, R. (1999) Redox reactions related to indoleamine 2,3-dioxygenase and tryptophan metabolism along the kynurenine pathway, *Redox Rep. 4*, 199−220.

BI060143J